Research Article | Vol. 11, No. 4 / 1 April 2020 / Biomedical Optics Express 2052

Biomedical Optics EXPRESS

Wide-field optical spectroscopy system integrating reflectance and spatial frequency domain imaging to measure attenuation-corrected intrinsic tissue fluorescence in radical prostatectomy specimens

EMILE BEAULIEU,[1,2] AUDREY LAURENCE,[1,2] MIRELA BIRLEA,[2,3] GUILLAUME SHEEHY,[1,2] LETICIA ANGULO-RODRIGUEZ,[1] MATHIEU LATOUR,[2,3] ROULA ALBADINE,[2,3] FRED SAAD,[2] DOMINIQUE TRUDEL,[2,3] AND FRÉDÉRIC LEBLOND[1,2,*]

[1] *Polytechnique Montreal, Dept. of Engineering Physics, C.P. 6079, Succ. Centre-ville, Montreal, QC H3C 3A7, Canada*
[2] *Centre Hospitalier Universitaire de Montreal Research Center (CRCHUM), 900 Rue Saint-Denis, Montreal, QC H2X 0A9, Canada*
[3] *University of Montreal, Dept. of Pathology and Cellular Biology, C.P. 6128, Succ. Centre-ville, Montreal, QC H3 T 1J4, Canada*
[*] *frederic.leblond@polymtl.ca*

Abstract: The development of a multimodal optical imaging system is presented that integrates endogenous fluorescence and diffuse reflectance spectroscopy with single-wavelength spatial frequency domain imaging (SFDI) and surface profilometry. The system images specimens at visible wavelengths with a spatial resolution of 70 µm, a field of view of 25 cm^2 and a depth of field of ~1.5 cm. The results of phantom experiments are presented demonstrating the system retrieves absorption and reduced scattering coefficient maps using SFDI with <6% reconstruction errors. A phase-shifting profilometry technique is implemented and the resulting 3-D surface used to compute a geometric correction ensuring optical properties reconstruction errors are maintained to <6% in curved media with height variations <20 mm. Combining SFDI-computed optical properties with data from diffuse reflectance spectra is shown to correct fluorescence using a model based on light transport in tissue theory. The system is used to image a human prostate, demonstrating its ability to distinguish prostatic tissue (anterior stroma, hyperplasia, peripheral zone) from extra-prostatic tissue (urethra, ejaculatory ducts, peri-prostatic tissue). These techniques could be integrated in robotic-assisted surgical systems to enhance information provided to surgeons and improve procedural accuracy by minimizing the risk of damage to extra-prostatic tissue during radical prostatectomy procedures and eventually detect residual cancer.

© 2020 Optical Society of America under the terms of the OSA Open Access Publishing Agreement

1. Introduction

Prostate cancer is the most common cancer in American men, and it is associated with increasing incidence rates [1–3]. Current prostate cancer clinical management guidelines are leading to an increasing number of instances where patients are submitted to active surveillance (low risk prostate cancer patients) and do not need to undergo surgery. However, surgery can be recommended for higher risk prostate cancers and in that case the only curative treatment is radical prostatectomy. There were more than 1300 radical prostatectomy procedures per million men in 2011 in the United States [4–7]. Worldwide, increasing numbers of radical prostatectomy

#388482 https://doi.org/10.1364/BOE.388482
Journal © 2020 Received 23 Jan 2020; revised 13 Feb 2020; accepted 8 Mar 2020; published 17 Mar 2020

Biomedical Optics EXPRESS

procedures are performed using robotic-assisted surgical systems, which can result in reduced side effects, increased normal tissue sparing, reduced loss of blood and shorter hospital stays [8,9].

Rates of remission following radical prostatectomy procedures are strongly influenced by the extent to which completeness of cancer resection is attained [10,11]. Because cancer frequently extends beyond the prostatic capsule [12], ensuring safety margins is often the adopted surgical strategy. The extent of surgical resection is then determined by multiple factors, including patient pre-surgical prostate-specific antigen (PSA) levels, clinical stage and pathological findings at diagnosis, as well as quality-of-life after the surgery [13–15]. Procedures are not only optimal when residual extra-prostatic cancer is avoided but also when damage to critical organs and structures, including bladder and nerves [16], is minimized. Less extended margins lower the risk of damage to surrounding tissue and increase post-procedure patient satisfaction by reducing side effects [17,18]. However, positive margins from un-resected cancer extending beyond the prostate decrease survival rates and lead to additional treatments [19,20]. As a result, radical prostatectomy procedures are performed by balancing the need to remove the entire prostate and leave no residual tumor tissue against the need to minimize healthy tissue damage.

Unlike surgical oncology approaches where co-registration methods with other imaging modalities are used to guide resection (*e.g.* magnetic resonance imaging (MRI) in brain cancer) [21], prostate cancer is usually not detectable using standard imaging techniques although MRI-based prostate cancer detection shows promises [22]. Surgeons thus typically rely on low accuracy methods, including prostate-specific antigen (PSA) testing and transrectal ultrasound (TRUS)-guided biopsies, to plan the procedure and determine target margin sizes pre-operatively [23]. As a result of the limitations of current prostate cancer diagnostic approaches, there is a need for new methods to enhance intraoperative tissue information through *in situ* tissue characterization.

Up until now, point probes were used to characterize prostate tissue using optical coherence tomography (OCT) [24], Raman spectroscopy [25], diffuse reflectance spectroscopy [26] as well as exogenous fluorescence from aminolevulinic acid-induced (ALA) protoporphyrin IX (PpIX) [27] and endogenous fluorescence [28]. All these approaches provided tissue imaging fields of view at mesoscopic scales *i.e.* of the order of one millimeter. Endogenous fluorescence results from tissue-native fluorescent molecules, thus giving access to molecular information without the need to inject a molecular tracer [29]. Although most intrinsic tissue fluorophore excitation bands are in the ultraviolet (UV), multiple molecules can still be detected through excitation above the UVA region (>380 nm) into the violet-blue part of the visible spectrum. Those include nicotinamide adenine dinucleotide (NADH) and flavins that can be used as a surrogate for cellular metabolism-associated mitochondrial activity [30,31]. Other fluorophores that can be excited with visible light include the structural proteins elastin and collagen as well as porphyrins, which were shown to accumulate specifically in some cancers [32]. Intrinsic tissue fluorescence detection has been achieved for multiple tissue types and pathologies [33], including for the detection of cancer in prostate and breast [34]. Although most work in mesoscopic intrinsic tissue fluorescence characterization was done with point probes, technologies were developed for macroscopic wide-field imaging in a limited number of oncology studies [35,36].

A practical limitation when attempting to detect intrinsic tissue fluorescence is the small quantum yields of fluorophores when compared to the cross-sections associated with absorption from tissue chromophores (*e.g.* hemoglobin and pigment molecules such as melanin) and elastic scattering from cell nuclei, membranes and organelles. These competing light interaction mechanisms affect the fluorescence signal, which is *non-quantitative* in the sense that tissue regions with a homogeneous concentration of fluorophores but with heterogeneous absorption/scattering properties could show different levels of detected fluorescence [37]. As a result, several mathematical models based on light transport in turbid media were developed for point-probe

Biomedical Optics EXPRESS

measurements to decouple absorption and scattering from fluorescence by applying an attenuation correction [38–40]. The objective in this line of research is to derive measures that are linearly related to the concentration of a fluorophore. This has been achieved for *in situ* brain tissue characterization when detecting ALA-induced PpIX with point-probes and wide-field imaging systems [41,42]. This work led to PpIX tissue concentration values C_{PpIX} decoupled from the effect of absorption and scattering. Applying the same methods to obtain *in situ* concentration values of intrinsic tissue fluorophores was attempted only in a limited number of studies but provided additional challenges because of the multiplicity of fluorescent markers contributing to the signal [43]. In fact, quantifying the concentration of each individual fluorescent marker would require the use of spectral de-convolution techniques but this has not been attempted yet for *in situ* endogenous macroscopic fluorescence detection.

Point-probe measurements typically offer fields of view of the order of 1 mm^2, which for some surgical applications can be insufficient for clinical adoption [44]. Thus, research groups have developed macroscopic attenuation-corrected fluorescence imaging techniques based on diffuse reflectance measurements [45]. In particular, the advent of spatial frequency domain imaging (SFDI) allowed the quantification of absorption/scattering properties across wide-field images which led to the development of light transport-based attenuation corrections adapted to wide-field imaging geometries [46–48]. This technique is called *attenuation-corrected fluorescence* (CF) imaging [49]. Such systems have been applied to PpIX quantification for skin cancer characterization [50,51], surgical guidance in neurosurgery [52,53] and photodynamic therapy (PDT) drug concentration monitoring [54]. Real-time CF imaging has also been attained in tissue phantoms [55].

Here we are presenting the development, detailed tissue phantoms characterization and preliminary in-human validation of a wide-field spectroscopic imaging system detecting reflectance spectra in the visible range as well as endogenous fluorescence from violet light excitation. The system also integrates SFDI to compute absorption/scattering coefficient maps and perform 3-D surface profiling. This information, along with reflectance and fluorescence spectra, is used in the scope of a light transport-based attenuation-corrected fluorescence (CF) model to compute a measure that can be used as a surrogate for the concentration of intrinsic tissue fluorescent molecules. The calibration and development process of the system leading to SFDI-reconstructed absorption and reduced scattering coefficients is presented with measurements in both low and high absorption Intralipid®-based optical phantoms. Measurements in solid phantoms are used to implement a profilometry correction accounting for sample geometry and the attenuation correction to fluorescence measurements is tested using liquid phantoms. Multimodal images are acquired in a human prostate following a radical prostatectomy procedure. Although cancer detection is not considered in the proof-of-principle study, basic statistical analyses applied to those images are presented providing preliminary evidence that biologically distinct prostate regions can be distinguished based on fluorescence, absorption and elastic scattering tissue optical properties. This work paves the way for a clinical study investigating the potential of the system in surgical guidance through residual cancer detection and normal tissue sparing during radical prostatectomy procedures.

2. Materials and methods

2.1. Multimodal imaging system

2.1.1. System hardware

The multimodal wide-field system was composed of a central detection branch surrounded by two distinct illumination branches, one for fluorescence & reflectance spectroscopy and one for single-wavelength SFDI (Fig. 1). Light detection was achieved using an sCMOS camera with a 4/3'' array composed of 2048×2048 pixels, each of dimensions 6.5×6.5 µm (C11440-22CU,

Biomedical Optics EXPRESS

Hamamatsu, Japan). The camera was connected through a relay lens to a liquid crystal tunable filter (LCTF) with operation range between 400 and 720 nm (VIS model, Varispec, USA) and a manually adjustable linear polarizer was introduced in the detection path to control tissue specular reflection. An aspherical objective (LM25XC, Kowa, USA) was used as the main interface for image acquisition.

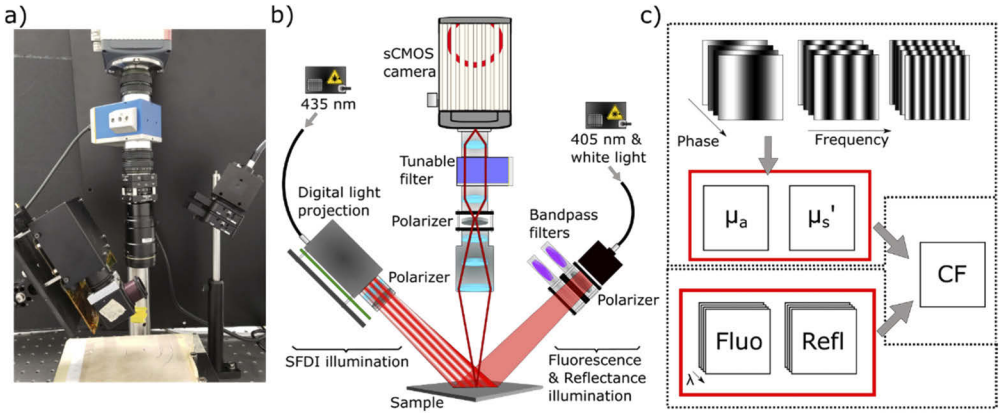

Fig. 1. (a) Photograph of the multimodal imaging system. (b) System schematics highlighting coupling optics and the two imaging branches allowing diffuse reflectance & fluorescence spectroscopy, single-wavelength SFDI and profilometry. (c) Flowchart representing the data acquisition and processing workflow.

Both illumination branches used the same light source consisting of seven high-power light emitting diodes (LED) centered at 405, 435, 475, 515, 550, 570 and 630 nm (79–536 mW, Spectra X model, Lumencor, USA) outputted through a 3 mm-diameter liquid light guide. The LEDs had overlapping spectra and could be powered simultaneously to emulate white light for diffuse reflectance spectroscopic imaging. Fluorescence spectroscopy was achieved using the 405 nm source and SFDI/profilometry using the 435 nm source. The 405 nm LED was used for fluorescence excitation since it overlapped with the extinction coefficient spectra of multiple endogenous fluorophores including NADH, flavins, porphyrins and elastin [56]. The liquid light guide output was collimated to ensure direct projection onto the sample. For reflectance & fluorescence, the source was connected to a two-slot optical rail allowing rapid switching between: i) a linear polarizer with optical axis manually adjusted to be at approximately 90° with respect to the linear polarizer in the detection branch, or ii) two successive 390 ± 40 nm OD > 6 bandpass filters (BrightLine FF01-390/40-25, Semrock, USA) used to cut off fluorescence excitation from the measurements. For SFDI, a light engine (CEL5500 model, DLI, USA) with a digital light processing chipset (DLP5500 model, Texas Instruments, USA) was used for spatial light modulation. The light engine casing was mechanically re-engineered to accommodate extra lenses, ensuring optical coupling with the liquid light guide. An adjustable linear polarizer was added to the light path providing an extra degree of freedom to limit signal contributions from specular reflections.

2.1.2. Acquisition control

Data acquisition was done using a custom LabVIEW program (National Instruments, USA) controlling the camera and LCTF parameters (number of spectral bands, spectral range, imaging time) for reflectance & fluorescence detection and pattern projection for SFDI measurements (spatial frequency and phase of sine waves). The software implemented an auto-exposure algorithm to adjust imaging time at each wavelength in order to maximize the signal-to-noise

Biomedical Optics EXPRESS

ratio (SNR). Reflectance & fluorescence spectroscopy measurements were acquired with the LCTF scanning from 420 to 650 nm with steps of 5 nm while SFDI data was acquired at a fixed LCTF wavelength centered at 435 nm.

2.2. System characterization and data processing

2.2.1. Imaging specifications

The spatial resolution of the system was determined by imaging a standard 1951 USAF resolution target and defined by the smallest element with distinct contrast. The depth of field was also determined using the resolution target, this time by varying the height of a z-axis stage on which the target was deposited to determine the range for which imaging can be achieved at a pre-specified spatial resolution associated with a 25% decrease when compared to the resolution evaluated at the focal plane. Because it was computed based on measurements in a non-diffusive material, the spatial resolution determined with the target must be considered a higher bound and its actual value in tissue is expected to degrade because of diffusion from elastic scattering.

2.2.2. SFDI data calibration and geometric optical properties correction

Spatial frequency domain imaging relies on projecting sine wave patterns at multiple spatial frequencies (k_x) and phases to extract the tissue modulation transfer function $M_{ac}(k_x)$ [57]. Because this transfer function is a function of tissue optical properties (absorption coefficient, μ_a, reduced scattering coefficient, μ_s'), tissue response can be measured at multiple frequencies to recover wide-field absorption and scattering images [58]. To account for the instrument response function, the technique requires the measured transfer function to be normalized against a reference measurement made on a sample with known tissue optical properties [59]. An intralipid®-based liquid phantom was used to compute the reference matrix function and white Monte Carlo simulations (Virtual photonics technology initiative, USA) used to create a lookup table for a large range of μ_a/μ_s couples under the hypothesis that the imaged geometry was a flat semi-infinite slab.

A correction algorithm was implemented to account for local sample height and curvature (i.e. angle associated with surface normal vectors), which can induce errors in reconstructed optical properties [60]. The profile-based correction method consists of normalizing the tissue transfer function using measured reference transfer functions for a range of distances consistent with expected height variations when imaging specimens [61]. Briefly, by measuring a reference transfer function at various heights and the corresponding phase, a relationship was found between phase variation the transfer function, which allowed to compute a correction factor for every imaged pixel. Angle correction was implemented by multiplying the reference matrix function with the cosine of the angle formed by the normal surface vector and the camera detection axis. The technique used four different phases since this was found to minimize artefacts in reconstructed 3-D profiles [62].

2.2.3. Fluorescence and reflectance data calibration

Figure 2 shows the calibration/normalization procedure applied to reflectance & fluorescence spectroscopy measurements to account for the instrument response function and produce attenuation-corrected fluorescence (CF) images. It included: i) a shading correction based on a reflectance standard (Spectralon, SRM-99, Labsphere, USA) measurement to compensate for inhomogeneities in the illumination field, and ii) a normalization with a spectral irradiance standard (63355, Newport, USA) to account for variations in system transmission across the spectral imaging domain. The shading correction for reflectance consists of a division by the normalized hyperspectral reflectance standard measurement. For fluorescence, the images were divided by a normalized intensity map of the standard's reflectance at 405 nm. Spectral response variations were accounted for by dividing all sample measurements by a correction

Biomedical Optics EXPRESS

curve corresponding to a hyperspectral measurement on the spectral irradiance standard divided by its theoretical spectrum.

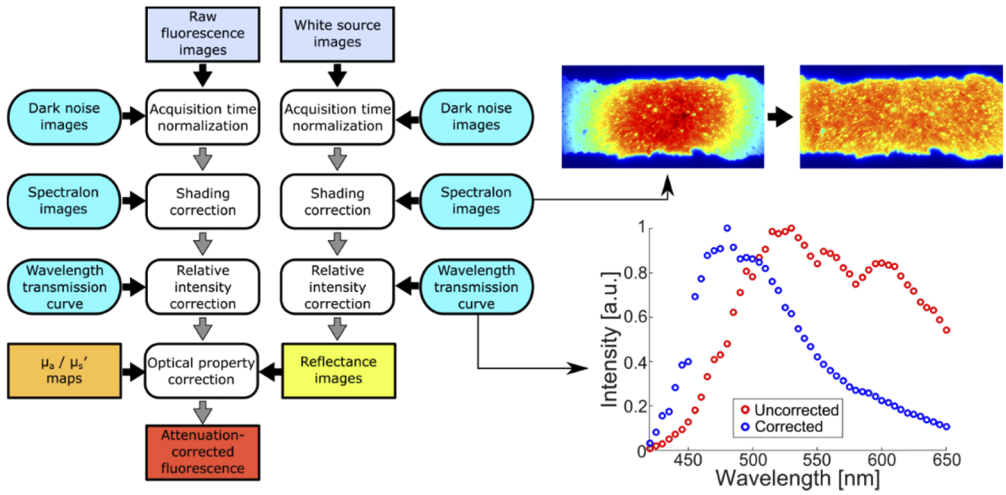

Fig. 2. Data processing flowchart for reflectance & fluorescence spectroscopy imaging. Also shown are representative images of a shading correction applied to a layer of fluorescent beads (excitation wavelength: 405 nm, emission wavelength: 505 nm, bead diameters: 255-500 µm, Cospheric, USA) as well as a representative relative intensity spectral correction associated with the instrument response.

2.2.4. Attenuation-corrected fluorescence

As the final processing step, a tissue light transport-based correction factor was computed and applied to the fluorescence images. The objective was to produce images in which the dependence of the measured fluorescence signals on elastic scattering and absorption from chromophores was reduced. The fluorescence attenuation correction at every point in the image was implemented using the SFDI-derived optical properties values and the spectroscopic reflectance measurement. The model developed by Kim et al. [63] for point probe measurements was used, which consists in modeling the attenuation-corrected fluorescence (CF) as

$$\mathrm{CF}(\lambda) = \left(\frac{\mu_{a,x}}{1 - R_{t,x}}\right)\left(\frac{F_{raw}(\lambda)}{R(\lambda)}\right), \tag{1}$$

where the experimental measurements are the fluorescence spectrum $F_{raw}(\lambda)$ and the reflectance spectrum $R(\lambda)$. The reflectance modeled by diffusion theory at the excitation wavelength, $R_{t,x}$, is a function of the internal reflection parameter κ and the reduced albedo a'. These coefficients depend on the refractive index of the sample ($n \cong 1.33$ for biological tissue [64]) as well as the absorption (μ_a) and reduced scattering (μ_s') coefficients at the excitation wavelength measured using SFDI.

In Eq. (1), the effect of absorption and scattering at the emission wavelength was approximated with a reflectance measurement $R(\lambda)$. This required that two conditions be satisfied: 1) the tissue absorption coefficient at excitation is significantly higher than its value at the emission wavelength, and 2) the fluorophore absorption at the excitation wavelength is negligible compared to tissue absorption from chromophores. Important absorbers in the prostate can be hemoglobin and the molecular constituents of seminal fluid [65]. However, for *ex vivo* measurements it is expected that seminal fluid could be the main absorber since blood concentration is much lower than under *in*

Biomedical Optics EXPRESS

vivo conditions. Both hemoglobin and seminal fluid have absorption peaks near the fluorescence excitation wavelength at 405 nm, with significantly lower values at higher wavelengths in the visible [66,67]. Moreover, although the extinction coefficients for intrinsic tissue fluorophores excited at 405 nm can be important, their absorption is usually orders of magnitude smaller when compared to tissue chromophores [33,42,51]. As a result, both conditions for validity of the CF model in Eq. (1) are expected to be satisfied in the prostate when measuring intrinsic tissue fluorescence.

Implementing Eq. (1) requires absorption & scattering properties at the fluorescence excitation wavelength (405 nm). However, the light transmission of both the LCTF and the digital light projector are low at that wavelength leading to poor SNR measurements. As a result, SFDI measurements were conducted instead at 435 nm where the transmission is ~3 times larger. This approximation is justified by the fact chromophore absorption coefficients peaked in the 400-435 nm region, which means absorption values at 405 and 435 nm will both be significantly higher than those at the emission wavelengths [66,67]. Consequently, although there may be a change in SFDI-derived optical properties between the two wavelengths it should not impact the validity of the correction.

2.3. SFDI and profilometry measurements

2.3.1. Low absorption tissue phantoms

Liquid optical phantoms made with water, Intralipid® (Sigma-Aldrich, USA) and food coloring dyes (McCormick, USA) were made to test the SFDI reconstruction capabilities. Theoretical values of the reduced scattering coefficient were obtained from the literature [68,69] while the absorption coefficient was measured using a custom single-point fibre optics spectrophotometer. A reference set of 72 optical phantoms was made with optical properties (at 435 nm) ranging from $\mu_a = 0.022$ mm^{-1} to 0.44 mm^{-1} and $\mu_s' = 0.72$ mm^{-1} to 2.16 mm^{-1}. The μ_s'/μ_a ratio in this phantom set ranged from 1.6 to 98.1, in most cases satisfying the diffusion approximation [70]. SFDI measurements were made for each phantom at 6 spatial frequencies ($k_x = 0.041$, 0.082, 0.123, 0.144, 0.164, and 0.246 mm^{-1}), each at 4 different phases ($\Delta\varphi = 0°$, 90°, 180°, 270°). The average power of the source over the imaging field of view was ~0.045 mW/cm^2. Reference phantoms with different optical properties were used to reconstruct optical properties maps for all phantoms and the average reconstructed properties across the imaging field were compared to the theoretical values to quantify reconstruction accuracy. Error bars were computed corresponding to the standard deviation of recovered optical properties across the imaging field. Only results associated with the reference phantom minimizing overall reconstruction errors were reported. Selection of the number of spatial frequencies and their specific values were pre-determined based on measurements in optical phantoms using 15 frequencies. Tests were performed evaluating different frequency subsets to determine combinations that minimized mean absorption and reduced scattering coefficients reconstruction errors.

2.3.2. High absorption tissue phantoms

The optical properties of the prostate are not expected to satisfy the diffusion approximation [71–73] since, e.g. the excitation source at 435 nm overlaps high hemoglobin absorption bands [67]. To validate SFDI in conditions closer to what is expected in prostate specimens, a second liquid phantom experiment was conducted in 8 phantoms with absorption ranging from $\mu_a = 0.22$ mm^{-1} to 1.32 mm^{-1} and reduced scattering ranging from $\mu_s' = 0.72$ mm^{-1} to 1.92 mm^{-1}. The μ_s'/μ_a ratio in those phantoms ranged from 3.0 to 1.0. SFDI measurements were made following the same protocol as for the low absorption phantoms. The data was processed using the same model and accuracy quantified using the same metrics. The results were used to guide the selection of an SFDI reference phantom maximizing μ_a and μ_s' reconstruction accuracy within an optical properties range representative of the prostate sample (high absorption).

Biomedical Optics EXPRESS

2.3.3. Profilometry measurements

An experiment using a solid phantom with homogeneous optical properties was devised to evaluate the profilometry technique by quantifying the impact of the geometric correction when applied to compute the optical properties of irregular surfaces. Using a PDMS base, the optical properties were varied using TiO_2 for scattering and nigrosin for absorption [74]. The solution was mixed and cast into three different mold shapes: a flat surface, a staircase with 8 steps of equal heights (total height: 24 mm) and a quarter of a sphere with a 2 cm radius. Four phantoms were fabricated: a flat surface with (μ_a, μ_s') = (0.06 mm^{-1}, 1.3 mm^{-1}), two staircases with (μ_a, μ_s') = (0.02 mm^{-1}, 0.88 mm^{-1}) and (μ_a, μ_s') = (0.026 mm^{-1}, 0.62 mm^{-1}), and a sphere quadrant with (μ_a, μ_s') = (0.025 mm^{-1}, 0.9 mm^{-1}) at 435 nm. Profilometry measurements were made at 435 nm with 4 phases ($\Delta\varphi = 0°$, 90°, 180°, 270°) at 8 spatial frequencies (k_x = 0.0041, 0.0165, 0.041, 0.082, 0.123, 0.144, 0.164, 0.246 mm^{-1}). The (μ_a, μ_s') = (0.026 mm^{-1}, 0.62 mm^{-1}) staircase phantom was imaged and reconstructed using the (μ_a, μ_s') = (0.02 mm^{-1}, 0.88 mm^{-1}) staircase phantom as reference. These measurements were used to characterize the performance of the height correction algorithm. The recovered optical properties values were averaged for each step of the staircase and the standard deviation computed to be reported as error bars. The maps of optical properties before and after applying the geometric correction were compared by computing the average optical properties reconstruction error for all steps of the staircase. The sphere quadrant was imaged and reconstructed with the flat surface as a reference to characterize the performance of the angle correction algorithm. An azimuthal angle θ was defined representing the angular difference between the surface normal vector and the detection axis of the camera. Regions of interest were defined corresponding to sections with $\Delta\theta = 5°$ intervals ranging from $\theta = 0$ to 50°. The same analysis that was applied to the staircase phantoms was applied to the quarter sphere section to evaluate the performance of the height and correction algorithms.

2.4. Fluorescence and reflectance spectroscopy tissue phantoms

Liquid phantoms were made to evaluate the CF technique using the fluorophore PpIX, which was chosen because it had an excitation band at 405 nm. For fluorescence, light fluence was ~4.5 mW/cm^2 while for reflectance, the sum of all LEDs amounted to ~15 mW/cm^2. In total, 9 optical phantoms were made with fluorophore concentrations 1.25, 2.5, 5 µg/ml, absorption coefficients μ_a = 0.05, 0.15, 0.25 mm^{-1} and reduced scattering μ_s' = 0.75, 1.15, 1.5 mm^{-1}. These phantoms were fabricated ensuring they satisfy the assumptions of the model in Eq. (1). Both reflectance and fluorescence measurements were made from 420 to 650 nm with steps of 5 nm (47 bands in total). SFDI measurements were made at 435 nm (~0.045 mW/cm^2) with 8 spatial frequencies (k_x = 0.0041, 0.0165, 0.041, 0.082, 0.123, 0.144, 0.164, 0.246 mm^{-1}) and 4 phases. To apply an attenuation correction to the fluorescence measurements, Eq. (1) was applied at each pixel and for each wavelength individually. The fluorescence (F_{raw}) and CF intensities of the 635 nm PpIX emission peak were averaged over the whole image and the standard deviation computed to be reported as an error bar. The performance of the attenuation correction technique was characterized by quantitatively evaluating the correlation factor R^2 between the real fluorophore concentration and either the raw fluorescence or the CF values [75].

2.5. Ex vivo human prostate imaging

A prostate specimen was imaged from a patient that underwent radical prostatectomy at the Centre Hospitalier de l'Université de Montréal (CHUM) and gave informed consent to participate in the institution's prostate cancer repository. Inclusion criteria were that preliminary biopsy results produced more than 2 positive cores with >10% of the core being cancerous and that excised prostates weighted more than 35 g. Following surgery, the whole organ was sent to the pathology ward where it was weighed, inked and identified according to institutional standards. A 10 mm thick slice was cut, placed between 2 cardboard sheets and immersed in 0.9% NaCl

Biomedical Optics EXPRESS

(4°C) prior to being transported to the optical imaging laboratory at the CHUM research center where the multimodal optical imaging system was located. Inspection of the slice allowed to determine it had surface height variations <4 mm and surface normal vectors with $\theta \leq \pm 25°$ except locally in the central prostate region (urethra) where $\theta > 50°$. Except for the urethra, these values are within the 24 mm height variations and 50° normal angle variations tested with the profilometry technique. A photograph of the prostate was taken followed by multimodal optical measurements with the system in <30 min. The specimen was then reintegrated into the standard pathology workflow. Inspection of the stained slices by a pathologist led to the identification of the following biologically distinct prostate regions: 1) anterior stroma, 2) urethra, 3) hyperplasia, 4) ejaculatory ducts, 5) peri-prostatic, 6) peripheral zone. The regions were then spatially registered with the spectroscopic/SFDI measurements as shown in Fig. 7.

Optical imaging was done using the same illumination/acquisition parameters and processing methods as for the phantom experiments in Section 2.4. To simplify data presentation and analysis, the reflectance, fluorescence and CF spectra were dimensionally reduced by computing the sum over all wavelengths at each image point. Imaging time was 4 s per band for reflectance and 5 s per band for fluorescence, totalling 188 s and 235 s, respectively. Due to high prostate absorption and limited illumination power (>2 orders of magnitude smaller than levels allowed for skin according to ANSI laser safety standards), 10 s exposure time was required for each SFDI spatial frequency and phase for a total of 320 s.

Reconstruction of absorption/scattering coefficients with SFDI was done using a transfer function computed based on measurements from the high absorption reference phantom. Optical properties (μ_a, μ_s' and CF) were averaged over each of the 6 prostate regions and univariate statistical analyses performed to test whether optically derived properties could be used to discriminate between regions. Specifically, a Kruskal-Wallis test was performed for each source of optical contrast between all prostate regions and boxplots were produced showing median (2nd quartile, Q2), 1st quartile (Q1), 3rd quartile (Q3), interquartile range (IQR), minimum value (Q1 - $1.5 \times$ IQR), maximum value (Q3 + $1.5 \times$ IQR) and outliers. Regions 1,3 and 6 were then grouped as prostatic tissue and regions 2,4 and 5 as extra-prostatic tissue. Boxplots were produced for these subgroups and a Kruskal-Wallis test performed to test the hypothesis that the two tissue categories could be distinguished.

3. Results

3.1. Characterization of the imaging system

Based on measurements from the resolution target, the system had a spatial resolution of 70 µm, a field of view of 5.5×5.5 cm and a depth of field of 1.5 cm. Although they were determined for non-diffusive media, these technical specifications are consistent with macroscopic whole prostate tissue interrogation at mesoscopic scales as well as with expected height variations when imaging prostate specimens.

3.2. SFDI and profilometry

3.2.1. Low absorption tissue phantoms

For each phantom, the SFDI-recovered optical properties (μ_a, μ_s') were averaged over the imaging field of view and the standard deviation computed. The reference phantom used for image reconstruction had $\mu_a = 0.05$ mm^{-1} and $\mu_s' = 1.2$ mm^{-1}. The average error (across all phantoms) from the theoretical values was 5.2% for absorption and 3.9% for scattering. Figure 3(a, b) shows the reconstructed optical properties for each phantom against the theoretical optical properties of the phantoms. The average standard deviation across the imaging field of view was 7.2% for μ_a and 3.6% for μ_s'. When restricting the optical properties to $\mu_a \leq 0.11$ mm^{-1}, average errors were 5.1% for μ_a and 3.2% for μ_s'. The average error on the excluded phantoms (0.17

Biomedical Optics EXPRESS

$mm^{-1} \leq \mu_a \leq 0.44\ mm^{-1}$) was 5.6% for μ_a and 5.5% for μ_s'. However, when using a reference phantom of 0.3 mm^{-1} absorption and 1 mm^{-1} reduced scattering on data from high absorption phantoms ($\mu_a > 0.11\ mm^{-1}$), average errors of 4.3% and 3.9% were obtained for μ_a and μ_s', respectively.

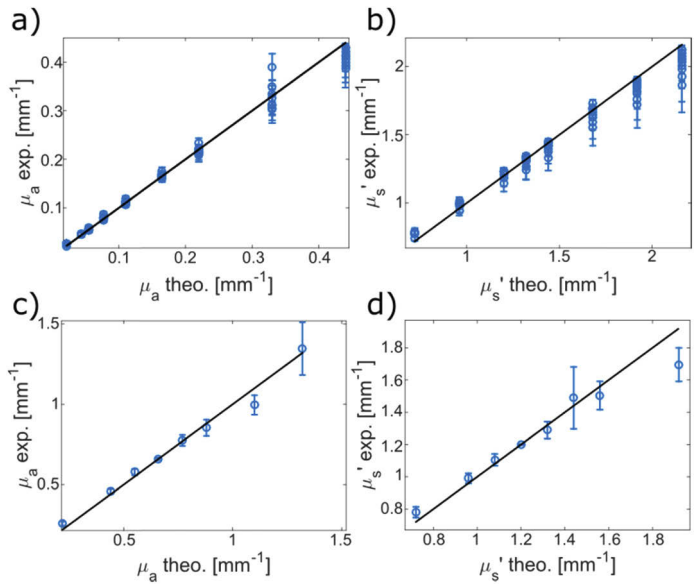

Fig. 3. Measured *vs.* theoretical optical properties: (a) absorption and (b) reduced scattering coefficients in the low absorption regime, (c) absorption and (b) reduced scattering coefficients in the high absorption regime. Each point in (a) and (c) is associated with a different scattering value whereas each point in (c) and (d) is associated to a different absorption value.

3.2.2. High absorption tissue phantoms

For high absorption phantom experiments, reconstructions were based on a reference phantom with $\mu_a = 0.66\ mm^{-1}$ and $\mu_s' = 1.1\ mm^{-1}$. The results are shown in Fig. 3(c, d). Average errors of 5.2% and 4.4% were obtained for absorption and reduced scattering, respectively. The average standard deviations were 5.2% and 5.0% for absorption and reduced scattering.

3.2.3. Profilometry

Implementation and validation of the profilometry correction algorithm to SFDI optical properties was done for both phantom shapes: staircase and quarter-sphere. Fig. 4(a, b) shows the SFDI-computed absorption and reduced scattering coefficients, respectively, on each step of the staircase with and without the geometric correction applied. The geometric correction allowed to reduce the average error on all steps due to height variations from 127% to 3.3% for absorption and from 28% to 2.5% for reduced scattering. Fig. 4(c, d) shows μ_a and μ_s' over all considered θ intervals on the quarter-sphere phantom with and without the geometric correction. The average error for all angles was reduced from 15.0% to 4.7% for absorption and from 5.8% to 2.9% for reduced scattering.

3.3. Fluorescence and reflectance spectroscopy

The attenuation-corrected fluorescence (CF), as well as the uncorrected fluorescence (F_{raw}) from the PpIX emission peak at 635 nm are shown in Fig. 5 as a function of the real fluorophore

Biomedical Optics EXPRESS

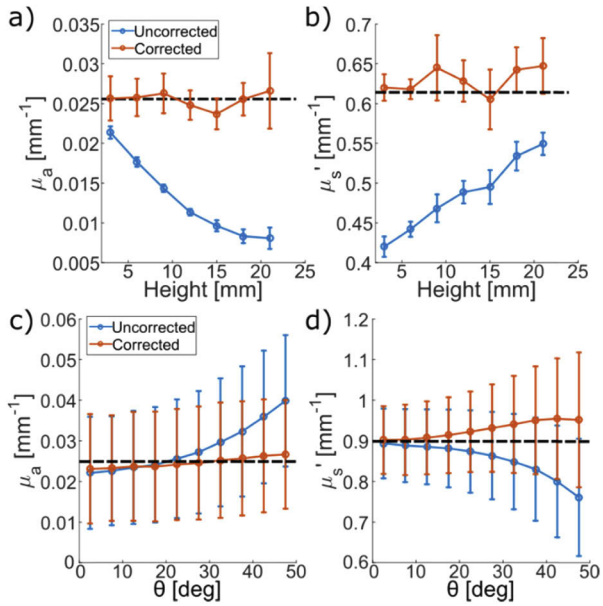

Fig. 4. (a) Absorption and (b) reduced scattering coefficients averages on staircase steps with and without the geometric correction. (c) Absorption and (d) reduced scattering coefficients averages computed on sections ($\Delta\theta = 5°$) of the quarter-sphere centered at an azimuthal angle θ with and without the geometric correction.

concentration (C_{PpIX}) in the phantoms. Figure 5(a) shows raw fluorescence measurements for all μ_a and μ_s' values evidencing almost no linear trend (correlation) with the theoretical PpIX concentration ($R^2 = 0.42$). This is because, for a given concentration of PpIX, different variations in absorption and scattering affect the level of detected light and can be misconstrued as variations in fluorophore concentration. However, Fig. 5(b) shows that using the CF model improved the correlation between real concentration and detected signals to $R^2 = 0.83$ from $R^2 = 0.42$ in the case of raw fluorescence.

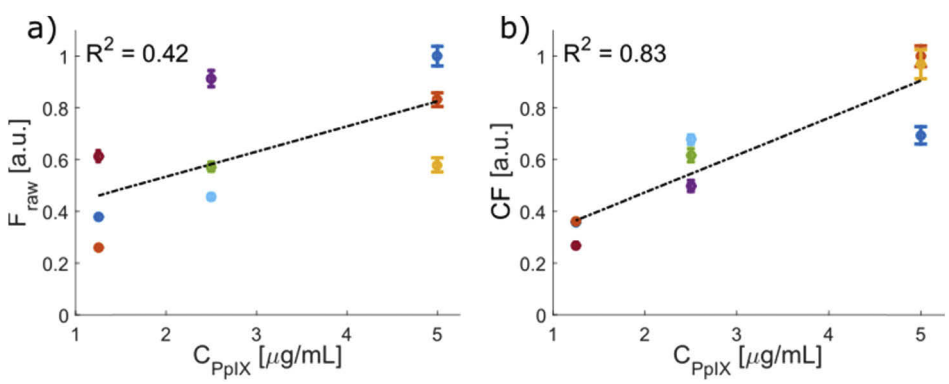

Fig. 5. Measured PpIX emission peak intensity as a function of the real PpIX concentration in liquid optical phantoms: (a) raw fluorescence and (b) attenuation-corrected fluorescence. Each phantom is represented by a point with a different color, each corresponding to a different value of absorption and reduced scattering coefficient.

Biomedical Optics EXPRESS

3.4. Ex vivo human prostate imaging

Figure 6 shows images of the prostate specimen slice for all optical modalities, including the absorption coefficient, the reduced scattering coefficient as well as the area under curve (AUC) -sum over all wavelengths- from reflectance, raw fluorescence and attenuation-corrected fluorescence (CF) spectra. The geometric correction from profilometry was applied to the SFDI optical properties maps. Reconstructed height variations of approximately 1 mm amplitude causing artificial striped patterns visible in the 3-D profile could be explained by stochastic noise causing inaccuracies in phase demodulation. Based on the results presented in section 3.2.3, erroneous variations of 1 mm height will introduce an error of approximately 5% in absorption and 2% in scattering coefficient maps; these numbers are comparable to the standard deviation obtained in flat phantoms (section 3.2.2). Thus, the impact of these noise-induced height artefacts should not exceed the expected variance in SFDI reconstruction. Overall, the effect of the profilometry correction on the μ_a and μ_s' profiles of the prostate was limited.

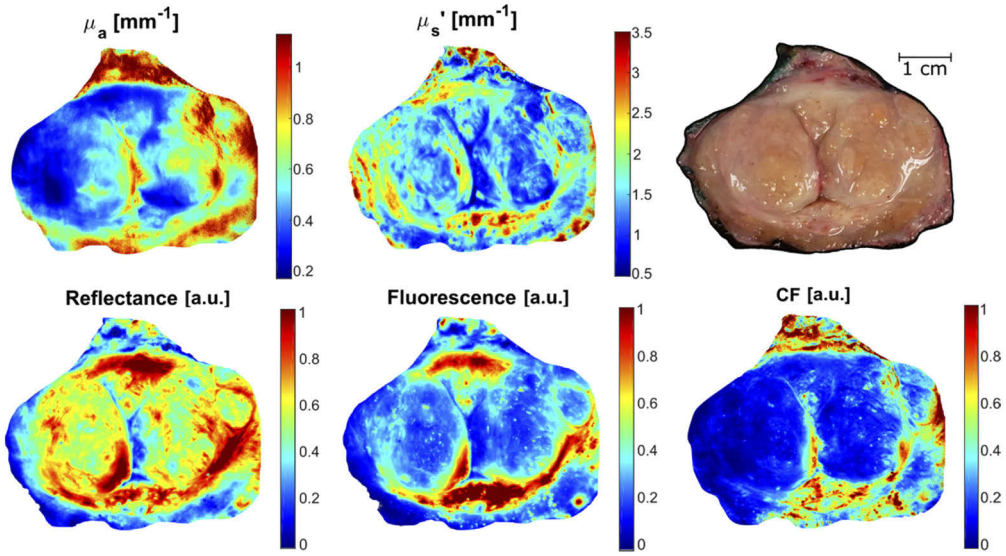

Fig. 6. Photograph (top right) and optical images of a prostate specimen slice in terms of the absorption coefficient, the reduced scattering coefficient and the integral under the curve of reflectance, raw fluorescence, and attenuation-corrected fluorescence (CF) spectra.

Figure 7 shows average reflectance, fluorescence and CF spectra for each of the 6 biologically distinct regions identified by the pathologist while Table 1 presents the average values and standard deviation for absorption, scattering, and CF spectrum AUC for these regions. The average SNR (over each region) per detection band for the reflectance signal is also reported to highlight potential decreases in signal quality in certain prostate regions. The SNR was computed as the square root of total detected light intensity assuming all measurements were shot noise (photonic noise) dominated. Figure 8 shows the boxplots associated with average SNR, absorption and reduced scattering coefficients as well as CF spectrum AUC. A Kruskal-Wallis test combined with pairwise comparisons demonstrated that, for all three sources of optical contrast, every region showed statistically significant differences from one another ($p < 0.01$). When conducting these statistical tests with F_{raw} instead of CF, $p < 0.01$ was also obtained. To highlight the impact of the geometric correction, Table S1 (Supplemental materials) shows the average values and standard deviation for absorption, scattering, and CF with and without

Biomedical Optics EXPRESS

the profilometry correction. The statistical tests also led to $p < 0.01$ without the profilometry correction.

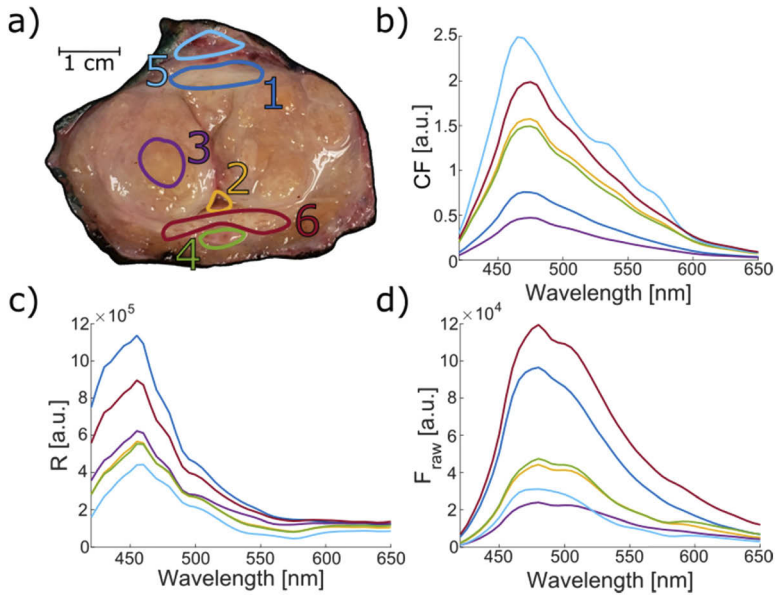

Fig. 7. (a) Photograph of the prostate specimen with biologically-distinct regions identified by a pathologist: 1) anterior stroma, 2) urethra, 3) hyperplasia, 4) ejaculatory ducts, 5) peri-prostatic, 6) peripheral zone. Average spectra computed for each region of interest. (b) Attenuation-corrected fluorescence (CF), (c) reflectance and (d) raw fluorescence. The colors of the contour delineations in (a) match the colors of their associated spectra in (b), (c) and (d).

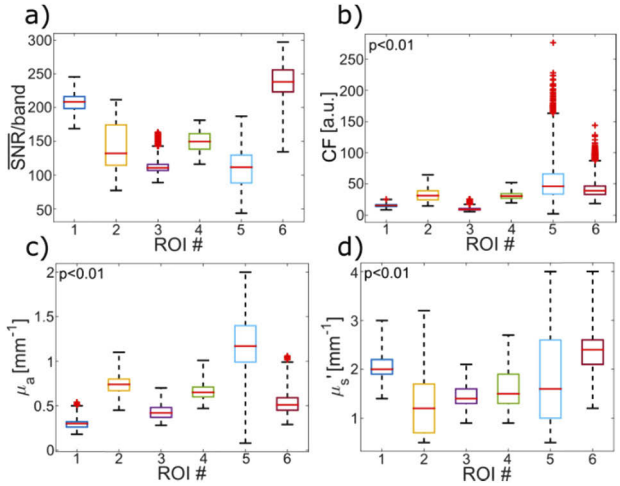

Fig. 8. Boxplots comparing (a) the SNR per spectral band, (b) the attenuation-corrected fluorescence (CF), (c) the absorption coefficient and (d) the reduced scattering coefficient of all prostate regions: 1) anterior stroma, 2) urethra, 3) hyperplasia, 4) ejaculatory ducts, 5) peri-prostatic, 6) peripheral zone. Outliers are represented by red crosses.

Biomedical Optics EXPRESS

Table 1. Average and standard deviation of the optical biomarkers for each region of the prostate specimen interrogated with the imaging system, including the number of image pixels over which they were computed and the signal-to-noise ratio (SNR) per spectral band.

Prostate region	# of pixels	Average SNR/band	CF [a.u.]	μ_a [mm^{-1}]	μ_s' [mm^{-1}]
Anterior stroma (1)	14432	207 ± 13	15.2 ± 2.4	0.30 ± 0.06	2.09 ± 0.24
Urethra (2)	1938	141 ± 35	32.6 ± 10.3	0.74 ± 0.09	1.23 ± 0.53
Hyperplasia (3)	28942	112 ± 8	9.7 ± 2.1	0.43 ± 0.07	1.44 ± 0.19
Ejaculatory ducts (4)	1498	149 ± 15	31.1 ± 5.0	0.66 ± 0.08	1.60 ± 0.38
Peri-prostatic (5)	9203	112 ± 31	53.1 ± 27.3	1.22 ± 0.31	1.88 ± 1.03
Peripheral zone (6)	19813	237 ± 28	40.9 ± 11.3	0.52 ± 0.10	2.43 ± 0.46

The data was further divided into prostatic (regions 1,3,6) and extra-prostatic tissue (regions 2,4,5) categories. Figure 9 shows the corresponding boxplots associated with average SNR, absorption and reduced scattering coefficient as well as CF. A Kruskal-Wallis test demonstrated that, for all three sources of optical contrast, prostatic and extra-prostatic tissue showed statistically significant differences from one another ($p < 0.01$). These statistical tests were also conducted and led to $p < 0.01$ without the profilometry correction and with F_{raw} instead of CF.

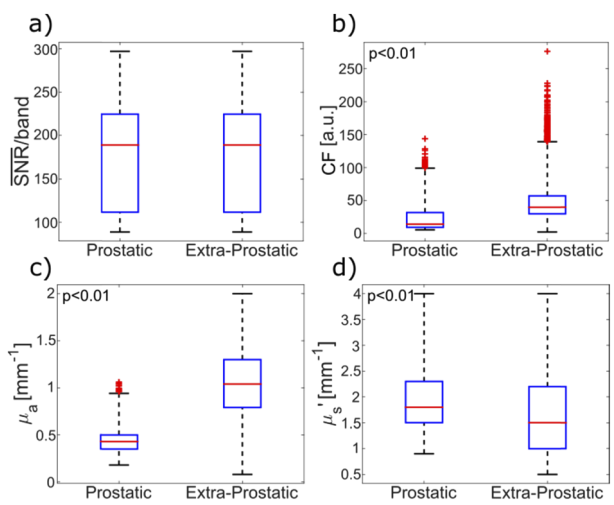

Fig. 9. Boxplots comparing (a) the SNR per spectral band, (b) the attenuation-corrected fluorescence (CF), (c) the absorption coefficient and (d) the reduced scattering coefficient between prostatic and extra-prostatic regions of the specimen. Outliers are represented as by red crosses.

4. Discussion and conclusions

This study presented the development and tissue phantoms validation of a multimodal wide-field imaging system as well as initial proof-of-concept *ex vivo* measurements in human prostate. This demonstrated new quantitative tissue biomarkers that could potentially distinguish biologically distinct regions, including prostatic *vs.* extra-prostatic structures. It is the first step in a larger-scale project aiming to automate tissue characterization during radical prostatectomy procedures to limit the risk of tissue damage and eventually assess whether optical spectroscopy can detect cancer that has invaded beyond the confines of the prostate organ.

Biomedical Optics EXPRESS

In the SFDI-based reconstruction of absorption and reduced scattering that was reported here, the average errors across both low and high absorption phantom experiments were similar to other studies [54,57,76–79]. However, there was a small increase in reconstruction error (+0.5%) for reduced scattering in the high absorption phantom set when compared to the low absorption set. It should be noted that part of the observed errors could be explained by inherent uncertainties associated with the properties used as *theoretical* values for the optical phantoms. For phantoms with $\mu_a = 0.17$ mm^{-1} to $\mu_a = 0.44$ mm^{-1}, reconstructions based on a reference phantom with $\mu_a = 0.05$ mm^{-1} led to increased errors (0.4% for μ_a, 1.6% for μ_s') when compared with the average errors computed over the whole phantoms set. When choosing a reference phantom with optical properties closer to the properties targeted for reconstruction ($\mu_a = 0.3$ mm^{-1}, $\mu_s' = 1$ mm^{-1}), reconstruction errors decreased by 1% when compared to the errors computed from the whole phantom set. This phenomenon was also observed in other work and highlights the importance of choosing a reference with optical properties as close as possible to the interrogated tissue associated with the biological application of interest [57]. Despite the reported decreases in performance for the high absorption phantom experiments, the reference phantom used for that dataset led to acceptable system performance across a range of absorption and reduced scattering coefficients representative of prostate samples.

The profilometry technique reduced the average error in absorption and elastic scattering by 124% and 25.5% respectively for a staircase phantom of 24 mm height. The reported errors of 3.3% and 2.5% for μ_a and μ_s' (after correction) were within the error margins of 5.8% and 2.9% for the reconstruction of the same optical properties in high absorption flat liquid phantoms. The increased size of the error bars in absorption and scattering (after the height correction was applied) were mainly caused by reconstructed height variations within each stair and could be a consequence of bubbles on the surface of the PDMS phantom.

For the sphere quadrant, in regions with the azimuthal angle $\theta \leq 50°$ the errors were reduced by 10.3% and 2.9% for μ_a and μ_s', respectively. The resulting errors of 4.7% and 2.9% (after correction) were within the expected 5.8% and 2.9% errors for the flat liquid phantoms with the same optical properties. However, the size of the error bars was unchanged after the correction possibly due to stochastic noise (less signal-to-noise ratio in high azimuthal angle regions) causing SFDI phase demodulation artefacts. To remove these artefacts, and potentially increase the azimuthal angle covered by the reconstruction, a different profilometry technique using higher spatial frequencies could be explored, although with these techniques obtaining absolute height values requires more involved calibration methods that may limit practical use during surgery [62,80]. The phantom results validate the efficiency of the 3-D profile to partially correct optical properties for geometrical features associated with height variations within the depth of field of the system if the curvature variations are associated with normal surface vector azimuthal angles <50°. An overall decrease in accuracy of reconstructed optical properties and reduced effectiveness of the geometric correction is expected for high curvature changes such as sharp depressions in the imaged specimens. This is for example the case for the central depression (urethra) in the imaged prostate specimen where the SFDI results could simply be excluded from further analyses.

In the fluorescent phantom studies, the calibration procedure and the attenuation correction model were able to correct for the instrument response function. The attenuation correction also reduced the impact of non-fluorescence attenuation factors despite the relatively larger spread in absorption and reduced scattering coefficients considered when compared to other PpIX quantification studies found in the literature [55,63,75,81]. The CF method significantly improved the correlation between theoretical PpIX concentration and the fluorescence intensity measurements from $R^2 = 0.42$ for raw fluorescence to $R^2 = 0.83$ for attenuation-corrected fluorescence.

Biomedical Optics EXPRESS

However, it was observed that fluorescence measurements from the lowest absorption phantom ($\mu_a = 0.05$ mm^{-1}, $\mu_s' = 0.75$ mm^{-1}) and the highest PpIX concentration was overcorrected by the CF method. In fluorescent phantoms the total absorption ($\mu_{a,tot}$) is the sum of chromophore absorption (μ_a from the food coloring dye) and fluorophore absorption (μ_{af} from PpIX), which is proportional to the concentration of the fluorescent molecule. Often in tissue $\mu_{a,tot} \approx \mu_a$ since $\mu_a >> \mu_{a,f}$, but for this low absorption phantom $\mu_{a,f}$ can no longer be neglected which is in breach of one of the validity conditions for Eq. (1). For this phantom, SFDI measurements lead to an absorption coefficient effectively larger than 0.05 mm^{-1}, which in turn leads to a lower CF intensity. However, this is not expected to be an issue for prostate measurements where fluorophore concentrations are low and lead to an effective absorption much smaller compared the absorption from chromophores [33,42,51].

A limitation of the CF method is that it does not account for the varying sampling depth associated with different emission wavelengths. As a result, CF values should be interpreted with the understanding that the CF spectrum AUC represents an effective fluorescence measurement averaged over depths sampled across the spectral detection range. Another potential limitation of the approach is that the attenuation correction may not be able to disentangle fluorescence from absorption and scattering with sufficiently high precision to detect subtle tissue biochemical modifications, including local pH changes. Using the sample average values $\mu_a = 0.52$ mm^{-1} and $\mu_s' = 1.71$ mm^{-1}, an estimation of imaging sampling depth could be obtained at 435 nm with a Monte-Carlo light transport modeling technique using as input parameters the average profile-corrected SFDI-computed optical properties of the prostate [82]. The resulting prediction is that 75% of the detected light came from the first 513 µm tissue layer, which corresponds to an average over all measured spatial frequencies.

The optical properties maps for the prostate specimen showed distinct features for absorption and reduced scattering, evidencing both phenomena were reconstructed with minimal optical contrast crosstalk. However, applying the profilometry-based geometric correction led only to minor changes in the optical properties maps, which is likely indicating that the height and curvature changes of the prostate specimen are too small to have a significant impact on the results. Overall, absorption values were high in the prostate and on average they were of the same order as reduced scattering, justifying the use of a high absorption reference phantom in SFDI reconstructions. There were important variations in optical properties within the imaged specimen, potentially resulting in uneven accuracies in optical properties reconstruction across the imaging field. This is because SFDI reconstruction accuracy decreases when the difference between absorption/scattering values of the imaged sample and those of the reference phantom increases. However, prostate optical properties values could not be found in literature at 435 nm for comparison; most studies measured absorption and scattering in the 600-1000 nm range [73].

Fluorescence and reflectance spectroscopy signals are not entirely uncorrelated, there were image features seen in the SFDI images that could also be seen in the spectroscopy images. As an example, the anterior stroma, which is characterized by a low absorption coefficient, also featured high reflectance and fluorescence. After applying the geometric correction and the fluorescence correction model, the resulting CF image was not visibly dependent on the SFDI-derived maps or any other geometrical features. The only still noticeable feature was the urethra geometric depression, representing only a small fraction of the sample. The fluorescence spectra acquired at each point in the image presented a similar shape to that of other studies for prostate tissue and other biological tissue excited at similar wavelengths [83,84]. However, the reflectance spectra did not present hemoglobin features, likely because the prostate measurements were made *ex vivo*. No studies imaging similar prostate specimens were found for comparison.

Statistical analyses of the prostate specimen images revealed that all pairwise comparisons between different regions had p-values indicative of significant differences for absorption, reduced scattering, and CF AUC. Note that while the dimensional reduction of CF simplifies results

Biomedical Optics EXPRESS

analysis it also reduces the informational content of the biomarker since several features on the spectrum could be used as features for differentiation. In the boxplots, the median can highlight absolute value differences in optical properties between regions, the IQR can be used as a surrogate for tissue heterogeneity and the maximum, minimum and number of outliers can be indicators of extreme variations in data that may have a biological origin but could also be attributable to low levels of SNR or artefacts due to the geometric correction not being able to fully account for tissue curvature changes. Most regions had noticeable differences in median values for all modalities. Although there were some exceptions, such as the urethra and ejaculatory ducts in CF, these differed significantly in IQR and maximum-minimum values. Peri-prostatic tissue tended to have higher variability but was also the region with the lowest SNR in reflectance signal, potentially explaining this observation. In general, CF had a smaller IQR compared to the other sources of optical contrast but it had the highest number of outliers. This could be traced back to the noise amplification due to mathematical operations (divisions and multiplications) required to apply the CF model. On the other end, absorption had more marked differences in median and IQR between regions than other modalities, implying chromophore concentrations varied importantly. It was also noted that μ_s' values had the highest heterogeneity for all regions. However, there was a significant variation in SNR between the regions, with several medians and IQR that prevented a straightforward visible interpretation of the results when comparing individual regions.

When comparing prostatic and extra-prostatic tissue, the p-values indicated that all modalities showed potential for differentiation. However, since the p-values were all $p < 0.01$ a direct comparison of the differentiation potential of the modalities could not be made. The low sample number also prevented a satisfactory analysis of the impact of the attenuation and profilometry corrections on classification, as initial tests showed F_{raw} and the optical properties without geometrical correction also attained $p < 0.01$. The difference in median was small for CF, but prostatic tissue presented a different Q1-Q2-Q3 distribution, had a smaller maximum-minimum range and fewer outliers. Absorption had significant median differences and values did not overlap in IQR. Reduced scattering presented a difference in medians and IQR. Furthermore, the SNR was very similar between the two categories, meaning differences between tissue categories were likely not due to noise-induced variability.

Further developments will be required to ensure utility of the multimodal imaging technique in a clinical/surgical setting. The current acquisition time for prostate specimen imaging was ~15 minutes which is unsuitable for surgical applications where information needs to be provided rapidly. However, a system redesign could decrease imaging time by at least 2 orders of magnitude by increasing illumination power, which is currently much lower than ANSI safety standards, and/or by replacing the LCTF (<10% transmission at lower visible wavelengths) with more effective filtering elements (*e.g.* interference filters). Another limitation of the system was that the profilometry technique and the geometric correction to SFDI-based reconstructions were only partially able to account for specimen height and curvature variations. In future system developments, this could be remedied either by considering a more accurate reconstruction technique using not only low frequency shifted patterns but also (in combination) high frequency patterns. Another solution could be envisioned where imaging is achieved with an imaging probe system making direct contact with the tissue. This would allow the surface to be rendered flat prior to imaging and, to a large extent, eliminate issues with specular reflections through index-matching between the tissue and a front-viewing imaging window.

The specimen imaging results preliminarily demonstrate the system's capacity to differentiate biologically distinct prostate regions. However, those findings were only based on one prostate implying no definite conclusions can be reached. A clinical study is being conducted involving a large number of radical prostatectomy patients where the goal is to quantitatively evaluate the potential of the optical biomarkers to differentiate biologically distinct normal/benign tissue

Biomedical Optics EXPRESS

regions but to also achieve cancer detection. To this end detailed dimensional reduction techniques (*e.g.* principal components analysis) will be used to determine the features most contributing to the variance of interest (*i.e.* extra prostatic *vs.* prostatic tissue, normal/benign *vs.* cancer) and machine learning models will be produced, validated and tested ensuring generalization to new data for live use during surgical procedures.

Future work will also tackle challenges relating with the presence of blood in the surgical cavity, which can dramatically attenuate optical signals and potentially make measurements, especially the absorption coefficient, non-specific to the tissue of interest. These effects could be partially addressed through a combination of surgeon training –to image only when blood pooling is minimal– and decrease in imaging time. This could be facilitated by the addition of another optical method for example intraoperative video-rate hemodynamic response assessment using a time-frequency associated with breathing to discriminate between blood pooling and blood vessels.

Funding

Natural Sciences and Engineering Research Council; TransMedTech Institute; Mitacs; Canadian Institutes of Health Research.

Acknowledgements

This work is supported by the TransMedTech Institute, the Discovery Grant program from Natural Sciences and Engineering Research Council of Canada (NSERC) and the Collaborative Health Research Program (CIHR and NSERC). Special thanks are extended to Sylvain Gioux of the University of Strasbourg for his help in the implementation of SFDI-based 3-D profile reconstruction and correction. The SFDI Monte-Carlo simulations were made possible through open-source software resources offered by the Virtual Photonics Technology Initiative, at the Beckman Laser Institute, University of California, Irvine.

Disclosures

No conflicts of interest, financial or otherwise, are declared by the authors.

References

1. M. M. Center, A. Jemal, J. Lortet-Tieulent, E. Ward, J. Ferlay, O. Brawley, and F. Bray, "International variation in prostate cancer incidence and mortality rates," Eur. Urol. **61**(6), 1079–1092 (2012).
2. A. W. Hsing, L. Tsao, and S. S. Devesa, "International comparisons of prostate cancer incidence and mortality," Int. J. Cancer **85**, 60–67 (2000).
3. C. G. Roehrborn and L. K. Black, "The economic burden of prostate cancer," BJU Int. **108**, 806–813 (2011).
4. S. R. Denmeade, J. T. Isaacs, S. R. Denmeade, J. T. Isaacs, and K. Comprehensive, "A history of prostate cancer treatment," Nat. Rev. Cancer **2**(5), 389–396 (2002).
5. A. Heidenreich, P. J. Bastian, J. Bellmunt, M. Bolla, S. Joniau, T. Van Der Kwast, M. Mason, V. Matveev, T. Wiegel, F. Zattoni, and N. Mottet, "EAU guidelines on prostate cancer. Part 1: Screening, diagnosis, and local treatment with curative intent - Update 2013," Eur. Urol. **65**(1), 124–137 (2014).
6. M. D. Tyson, P. E. Andrews, R. F. Ferrigni, M. R. Humphreys, A. S. Parker, and E. P. Castle, "Radical Prostatectomy Trends in the United States: 1998 to 2011," Mayo Clin. Proc. **91**(1), 10–16 (2016).
7. J. A. Halpern, J. E. Shoag, A. S. Artis, K. V. Ballman, A. Sedrakyan, D. L. Hershman, J. D. Wright, Y. C. T. Shih, and J. C. Hu, "National trends in prostate biopsy and radical prostatectomy volumes following the us preventive services task force guidelines against prostate-specific antigen screening," JAMA Surg. **152**(2), 192–198 (2017).
8. D. V. Makarov, J. B. Yu, R. A. Desai, D. F. Penson, and C. P. Gross, "The association between diffusion of the surgical robot and radical prostatectomy rates," Med. Care **49**(4), 333–339 (2011).
9. V. Ficarra, G. Novara, W. Artibani, A. Cestari, A. Galfano, M. Graefen, G. Guazzoni, B. Guillonneau, M. Menon, F. Montorsi, V. Patel, J. Rassweiler, and H. Van Poppel, "Retropubic, Laparoscopic, and Robot-Assisted Radical Prostatectomy: A Systematic Review and Cumulative Analysis of Comparative Studies," Eur. Urol. **55**(5), 1037–1063 (2009).

Biomedical Optics EXPRESS

10. G. D. Grossfeld, J. J. CHang, J. M. Broering, D. P. Miller, J. Yu, S. C. Flanders, J. M. Henning, D. M. Stier, and P. R. Carroll, "Impact of Positive Surgical Margins on Prostate Cancer Recurrence and the Use of Secondary Cancer Treatment: Data From the Capsure Database," J. Urol. **163**(4), 1171–1177 (2000).
11. I. D. Nagtegaal, C. A. M. Marijnen, E. K. Kranenbarg, C. J. H. Van De Velde, J. Han, and J. M. Van Krieken, "Circumferential Margin Involvement Is Still an Important Predictor of Local Recurrence in Rectal Carcinoma Not One Millimeter but Two Millimeters Is the Limit," Am. J. Surg. Pathol. **26**(3), 350–357 (2002).
12. B. J. Davis, T. M. Pisansky, T. M. Wilson, H. J. Rothenberg, A. Pacelli, D. W. Hillman, D. J. Sargent, and D. G. Bostwick, "The radial distance of extraprostatic extension of prostate carcinoma," Cancer **85**, 2630–2637 (1999).
13. A. Nakao, S. Takeda, M. Sakai, T. Kaneko, S. Inoue, H. Sugimoto, and N. Kanazumi, "Extended Radical Resection Versus Standard Resection for," Pancreas **28**(3), 289–292 (2004).
14. C. Urban, P. C. Rey, G. Gatti, A. Luini, F. De Lorenzi, M. Rietjens, J.-Y. Petit, F. Maffini, and N. Kaur, "Comparative Study of Surgical Margins in Oncoplastic Surgery and Quadrantectomy in Breast Cancer," Ann. Surg. Oncol. **12**(7), 539–545 (2005).
15. W. Stummer, J.-C. Tonn, H. M. Mehdorn, U. Nestler, K. Franz, C. Goetz, A. Bink, and U. Pichlmeier, "Counterbalancing risks and gains from extended resections in malignant glioma surgery: a supplemental analysis from the randomized 5-aminolevulinic acid glioma resection study," J. Neurosurg. **114**(3), 613–623 (2011).
16. J. Holzbeierlein, M. Peterson, and J. A. Smith, "Variability of results of cavernous nerve stimulation during radical prostatectomy," J. Urol. **165**(1), 108–110 (2001).
17. M. G. Sanda, R. L. Dunn, J. Michalski, H. M. Sandler, L. Northouse, L. Hembroff, X. Lin, T. K. Greenfield, M. S. Litwin, C. S. Saigal, A. Mahadevan, E. Klein, A. Kibel, L. L. Pisters, D. Kuban, I. Kaplan, D. Wood, J. Ciezki, N. Shah, and J. T. Wei, "Quality of Life and Satisfaction with Outcome among Prostate-Cancer Survivors," N. Engl. J. Med. **358**(12), 1250–1261 (2008).
18. J. L. Stanford, A. S. Hamilton, F. D. Gilliland, R. A. Stephenson, J. W. Eley, P. C. Albertsen, L. C. Harlan, and A. L. Potosky, "After Radical Prostatectomy for Clinically Localized Prostate Cancer The Prostate Cancer Outcomes Study," **1024**, (2015).
19. O. Yossepowitch, A. Bjartell, J. A. Eastham, M. Graefen, B. D. Guillonneau, P. I. Karakiewicz, R. Montironi, and F. Montorsi, "Positive Surgical Margins in Radical Prostatectomy: Outlining the Problem and Its Long-Term Consequences," Eur. Urol. **55**(1), 87–99 (2009).
20. M. L. Blute, D. G. Bostwick, E. J. Bergstralh, J. M. Slezak, S. K. Martin, C. L. Amling, and H. Zincke, "Anatomic site-specific positive margins in organ-confined prostate cancer and its impact on outcome after radical prostatectomy," Urology **50**(5), 733–739 (1997).
21. D. A. Orringer, A. Golby, and F. Jolesz, "Neuronavigation in the surgical management of brain tumors: Current and future trends," Expert Rev. Med. Devices **9**(5), 491–500 (2012).
22. G. Ayala, J. A. Tuxhorn, T. M. Wheeler, A. Frolov, P. T. Scardino, M. Ohori, M. Wheeler, J. Spitler, and D. R. Rowley, "Reactive Stroma as a Predictor of Biochemical-Free Recurrence in Prostate Cancer," Clin. Cancer Res. **9**(13), 4792–4801 (2003).
23. K. Aubertin, V. Q. Trinh, M. Jermyn, P. Baksic, A. Grosset, J. Desroches, K. St-arnaud, M. Birlea, M. Vladoiu, and M. Latour, "Mesoscopic characterization of prostate cancer using Raman spectroscopy: potential for diagnostics and therapeutics," BJU Int. **122**(2), 326–336 (2018).
24. S. Rais-Bahrami, A. W. Levinson, N. M. Fried, G. A. Lagoda, A. Hristov, Y. Chuang, A. L. Burnett, and L. M. Su, "Optical Coherence Tomography of Cavernous Nerves: A Step Toward Real-Time Intraoperative Imaging During Nerve-Sparing Radical Prostatectomy," Urology **72**(1), 198–204 (2008).
25. P. Crow, N. Stone, C. A. Kendall, J. S. Uff, J. A. M. Farmer, H. Barr, and M. P. J. Wright, "The use of Raman spectroscopy to identify and grade prostatic adenocarcinoma in vitro," Br. J. Cancer **89**(1), 106–108 (2003).
26. O. M. A'Amar, L. Liou, E. Rodriguez-Diaz, A. De Las Morenas, and I. J. Bigio, "Comparison of elastic scattering spectroscopy with histology in ex vivo prostate glands: Potential application for optically guided biopsy and directed treatment," Lasers Med. Sci. **28**(5), 1323–1329 (2013).
27. D. Zaak, R. Sroka, W. Khoder, C. C. Adam, S. Tritschler, A. Karl, O. Reich, R. Knuechel, R. Baumgartner, D. Tilki, G. Popken, A. Hofstetter, and C. G. Stief, "Photodynamic Diagnosis of Prostate Cancer Using 5-Aminolevulinic Acid—First Clinical Experiences," Urology **72**(2), 345–348 (2008).
28. J. Ebenezar, Y. Pu, W. Wang, Y. Yang, and R. R. Alfano, "Stokes shift spectroscopy pilot study for cancerous and normal prostate tissues," Opt. Lett. **37**(16), 3360 (2012).
29. G. Marriott, R. M. Clegg, D. J. Arndt-Jovin, and T. M. Jovin, "Time resolved imaging microscopy. Phosphorescence and delayed fluorescence imaging," Biophys. J. **60**(6), 1374–1387 (1991).
30. K. Koenig and H. Schneckenburger, "Laser-induced autofluorescence for medical diagnosis," J. Fluoresc. **4**(1), 17–40 (1994).
31. L. Z. Li, "Imaging mitochondrial redox potential and its possible link to tumor metastatic potential," J. Bioenerg. Biomembr. **44**(6), 645–653 (2012).
32. V. Masilamani, K. Al-Zhrani, M. Al-Salhi, A. Al-Diab, and M. Al-Ageily, "Cancer diagnosis by autofluorescence of blood components," J. Lumin. **109**(3-4), 143–154 (2004).
33. G. A. Wagnieres, W. M. Star, and B. C. Wilson, "In Vivo Fluorescence Spectroscopy and Imaging for Oncological Applications of Technology," Photochemistry **68**(5), 603–632 (1998).

Biomedical Optics EXPRESS

34. Y. Pu, W. Wang, Y. Yang, and R. R. Alfano, "Stokes shift spectroscopic analysis of multifluorophores for human cancer detection in breast and prostate tissues," J. Biomed. Opt. **18**(1), 017005 (2013).
35. J. Haringsma and G. N. J. Tytgat, "Fluorescence and autofluorescence," Best Pract. Res., Clin. Gastroenterol. **13**(1), 1–10 (1999).
36. A. M. Kluftinger, N. L. Davis, N. F. Quenville, S. Lam, J. Hung, and B. Palcic, "Detection of squamous cell cancer and pre-cancerous lesions by imaging of tissue autofluorescence in the hamster cheek pouch model," Surg. Oncol. **1**(2), 183–188 (1992).
37. R. Richards-Kortum and E. Sevick-Muraca, "Quantitative Optical Spectroscopy for Tissue Diagnosis," Annu. Rev. Phys. Chem. **47**(1), 555–606 (1996).
38. M. S. Patterson and B. W. Pogue, "Mathematical model for time-resolved and frequency-domain fluorescence spectroscopy in biological tissues," Appl. Opt. **33**(10), 1963–1974 (1994).
39. K. Vishwanath, B. Pogue, and M. A. Mycek, "Quantitative fluorescence lifetime spectroscopy in turbid media: Comparison of theoretical, experimental and computational methods," Phys. Med. Biol. **47**(18), 3387–3405 (2002).
40. B. W. Pogue and G. Burke, "Fiber-optic bundle design for quantitative fluorescence measurement from tissue," Appl. Opt. **37**(31), 7429–7436 (1998).
41. P. A. Valdés, F. Leblond, A. Kim, B. T. Harris, B. C. Wilson, and X. Fan, "Quantitative fluorescence in intercranial tumor: implications for ALA-induced PpIX as an intraoperative bioamarer," J. Neurosurg. **115**(1), 11–17 (2011).
42. P. A. Valdés, A. Kim, F. Leblond, O. M. Conde, B. T. Harris, K. D. Paulsen, B. C. Wilson, and D. W. Roberts, "Combined fluorescence and reflectance spectroscopy for in vivo quantification of cancer biomarkers in low- and high-grade glioma surgery," J. Biomed. Opt. **16**(11), 116007 (2011).
43. P. A. Valdés, F. Leblond, V. L. Jacobs, B. C. Wilson, K. D. Paulsen, and D. W. Roberts, "Quantitative, spectrally-resolved intraoperative fluorescence imaging," Sci. Rep. **2**(1), 798 (2012).
44. B. A. Flusberg, E. D. Cocker, W. Piyawattanametha, J. C. Jung, E. L. M. Cheung, and M. J. Schnitzer, "Fiber-optic fluorescence imaging," Nat. Methods **2**(12), 941–950 (2005).
45. R. S. Bradley and M. S. Thorniley, "A review of attenuation correction techniques for tissue fluorescence," J. R. Soc. Interface **3**(6), 1–13 (2006).
46. J. Wu, M. S. Feld, and R. P. Rava, "Analytical model for extracting intrinsic fluorescence in turbid media," Appl. Opt. **32**(19), 3585 (1993).
47. Q. Zhang, M. Muller, J. Wu, and M. Feld, "Turbidity-free fluorescence spectroscopy of biological tissue," Opt. Lett. **25**(19), 1451–1453 (2000).
48. C. M. Gardner, S. L. Jacques, and A. J. Welch, "Fluorescence spectroscopy of tissue: recovery of intrinsic fluorescence from measured fluorescence," Appl. Opt. **35**(10), 1780 (1996).
49. B. Yang, M. Sharma, and J. W. Tunnell, "Attenuation-corrected fluorescence extraction for image-guided surgery in spatial frequency domain," J. Biomed. Opt. **18**(8), 080503 (2013).
50. R. B. Saager, D. J. Cuccia, S. Saggese, K. M. Kelly, and A. J. Durkin, "Quantitative fluorescence imaging of protoporphyrin IX through determination of tissue optical properties in the spatial frequency domain," J. Biomed. Opt. **16**(12), 126013 (2011).
51. U. Sunar, D. J. Rohrbach, J. Morgan, N. Zeitouni, and B. W. Henderson, "Quantification of PpIX concentration in basal cell carcinoma and squamous cell carcinoma models using spatial frequency domain imaging," Biomed. Opt. Express **4**(4), 531 (2013).
52. M. Sibai, I. Veilleux, J. T. Elliott, F. Leblond, and B. C. Wilson, "Quantitative spatial frequency fluorescence imaging in the sub-diffusive domain for image-guided glioma resection," Biomed. Opt. Express **6**(12), 4923 (2015).
53. P. A. Valdés, D. W. Roberts, F. Lu, and A. Golby, "Optical technologies for intraoperative neurosurgical guidance," Neurosurg. Focus **40**(3), E8 (2016).
54. J. Kress, D. J. Rohrbach, K. A. Carter, D. Luo, C. Poon, S. Aygun-Sunar, S. Shao, S. Lele, J. F. Lovell, and U. Sunar, "A dual-channel endoscope for quantitative imaging, monitoring, and triggering of doxorubicin release from liposomes in living mice," Sci. Rep. **7**(1), 15578 (2017).
55. P. A. Valdés, J. P. Angelo, H. S. Choi, and S. Gioux, "qF-SSOP: real-time optical property corrected fluorescence imaging," Biomed. Opt. Express **8**(8), 3597 (2017).
56. N. Ramanujam, "Fluorescence Spectroscopy of Neoplastic and Non-Neoplastic Tissues," Neoplasia **2**(1-2), 89–117 (2000).
57. D. J. Cuccia, F. Bevilacqua, A. J. Durkin, F. R. Ayers, and B. J. Tromberg, "Quantitation and mapping of tissue optical properties using modulated imaging," J. Biomed. Opt. **14**(2), 024012 (2009).
58. N. Bodenschatz, P. Krauter, A. Liemert, J. Wiest, and A. Kienle, "Model-based analysis on the influence of spatial frequency selection in spatial frequency domain imaging," Appl. Opt. **54**(22), 6725 (2015).
59. J. P. Angelo, S.-J. Chen, M. Ochoa, U. Sunar, S. Gioux, X. Intes, S.-J. Chen, M. Ochoa, U. Sunar, and S. Gioux, "Review of structured light in diffuse optical imaging," J. Biomed. Opt. **24**(07), 1 (2018).
60. N. Bodenschatz, A. Brandes, A. Liemert, and A. Kienle, "Sources of errors in spatial frequency domain imaging of scattering media," J. Biomed. Opt. **19**(7), 071405 (2014).
61. S. Gioux, A. Mazhar, D. J. Cuccia, A. J. Durkin, B. J. Tromberg, and J. V. Frangioni, "Three-dimensional surface profile intensity correction for spatially modulated imaging," J. Biomed. Opt. **14**(3), 034045 (2009).

Biomedical Optics EXPRESS

62. L. Angulo-rodriguez, Y. Badawy, and F. Leblond, "Development and Validation of Phase-Shifting Profilometry Using a Hyperspectral Spatial Frequency Domain Imaging System Integrated with a Neurosurgical Microscope," J. Bioeng. Biomed. Sci. **9**, 1000257 (2019).
63. A. Kim, Y. Moriyama, and B. C. Wilson, "Quantification of in vivo fluorescence decoupled from the effects of tissue optical properties using fiber-optic spectroscopy measurements," J. Biomed. Opt. **15**(01), 1–12 (2010).
64. S. L. Jacques, "Optical properties of biological tissues: a review," Phys. Med. Biol. **58**(11), R37–R61 (2013).
65. S. Grabtchak, L. G. Montgomery, and W. M. Whelan, "Feasibility of interstitial near-infrared radiance spectroscopy platform for ex vivo canine prostate studies: optical properties extraction, hemoglobin and water concentration, and gold nanoparticles detection," J. Biomed. Opt. **19**(5), 057003 (2014).
66. W. Lee and B. Khoo, "Forensic light sources for detection of biological evidences in crime scene investigation: a review," Malaysian J. Forensic Sci. **1**, 17–27 (2010).
67. J. L. Sandell and T. C. Zhu, "A review of in-vivo optical properties of human tissues and its impact on PDT," J. Biophotonics **4**, 773–787 (2011).
68. T. Phantoms, P. Di Ninni, F. Martelli, and G. Zaccanti, "Intralipid: Towards a diffusive reference standard for optical," Phys. Med. Biol. **56** (2011).
69. L. Spinelli, M. Botwicz, N. Zolek, M. Kacprzak, D. Milej, P. Sawosz, A. Liebert, U. Weigel, T. Durduran, F. Foschum, A. Kienle, F. Baribeau, S. Leclair, J.-P. Bouchard, I. Noiseux, P. Gallant, O. Mermut, A. Farina, A. Pifferi, A. Torricelli, R. Cubeddu, H.-C. Ho, M. Mazurenka, H. Wabnitz, K. Klauenberg, O. Bodnar, C. Elster, M. Bénazech-Lavoué, Y. Bérubé-Lauzière, F. Lesage, D. Khoptyar, A. A. Subash, S. Andersson-Engels, P. Di Ninni, F. Martelli, and G. Zaccanti, "Determination of reference values for optical properties of liquid phantoms based on Intralipid and India ink," Biomed. Opt. Express **5**(7), 2037 (2014).
70. T. A. Erickson, A. Mazhar, D. Cuccia, A. J. Durkin, and J. W. Tunnell, "Lookup-table method for imaging optical properties with structured illumination beyond the diffusion theory regime," J. Biomed. Opt. **15**(3), 036013 (2010).
71. A. A. Oraevsky, S. L. Jacques, and F. K. Tittel, "Measurement of tissue optical properties by time-resolved detection of laser-induced transient stress," Appl. Opt. **36**(1), 402 (1997).
72. T. Svensson and S. Andersson-engels, "In vivo optical characterization of human prostate tissue using near-infrared time-resolved spectroscopy," J. Biomed. Opt. **12**(1), 014022 (2007).
73. D. Piao, K. E. Bartels, Z. Jiang, G. R. Holyoak, J. W. Ritchey, G. Xu, C. F. Bunting, and G. Slobodov, "Alternative transrectal prostate imaging: A diffuse optical tomography method," IEEE J. Sel. Top. Quantum Electron. **16**(4), 715–729 (2010).
74. B. W. Pogue and M. S. Patterson, "Review of tissue simulating phantoms for optical spectroscopy, imaging and dosimetry," J. Biomed. Opt. **11**(4), 041102 (2006).
75. P. A. Valdés, F. Leblond, A. Kim, B. C. Wilson, K. D. Paulsen, and D. W. Roberts, "A spectrally constrained dual-band normalization technique for protoporphyrin IX quantification in fluorescence-guided surgery," Opt. Lett. **37**(11), 1817 (2012).
76. M. Sibai, I. Veilleux, J. T. Elliott, F. Leblond, D. W. Roberts, and B. C. Wilson, "Quantitative fluorescence imaging enabled by spatial frequency domain optical-property mapping in the sub-diffusive regime for surgical guidance," Prog. Biomed. Opt. Imaging - Proc. SPIE **9311** (2015).
77. S. Tabassum, Y. Zhao, R. Istfan, J. Wu, D. J. Waxman, and D. Roblyer, "Feasibility of spatial frequency domain imaging (SFDI) for optically characterizing a preclinical oncology model," Biomed. Opt. Express **7**(10), 4154–4170 (2016).
78. J. R. Weber, D. J. Cuccia, W. R. Johnson, G. H. Bearman, A. J. Durkin, M. Hsu, A. Lin, D. K. Binder, D. Wilson, and B. J. Tromberg, "Multispectral imaging of tissue absorption and scattering using spatial frequency domain imaging and a computed-tomography imaging spectrometer," J. Biomed. Opt. **16**(1), 011015 (2011).
79. A. M. Laughney, V. Krishnaswamy, T. B. Rice, D. J. Cuccia, R. J. Barth, B. J. Tromberg, K. D. Paulsen, B. W. Pogue, and W. A. Wells, "System analysis of spatial frequency domain imaging for quantitative mapping of surgically resected breast tissues," J. Biomed. Opt. **18**(3), 036012 (2013).
80. J.-S. Hyun and S. Zhang, "Enhanced two-frequency phase-shifting method," Appl. Opt. **55**(16), 4395–4401 (2016).
81. A. St-Georges-Robillard, M. Masse, M. Cahuzac, M. Strupler, B. Patra, A. M. Orimoto, J. Kendall-Dupont, B. Péant, A. M. Mes-Masson, F. Leblond, and T. Gervais, "Fluorescence hyperspectral imaging for live monitoring of multiple spheroids in microfluidic chips," Analyst **143**(16), 3829–3840 (2018).
82. C. K. Hayakawa, K. Karrobi, V. Pera, D. Roblyer, and V. Venugopalan, "Optical sampling depth in the spatial frequency domain," J. Biomed. Opt. **24**(07), 1 (2018).
83. Y. Pu, W. Wang, G. Tang, and R. R. Alfano, "Changes of collagen and nicotinamide adenine dinucleotide in human cancerous and normal prostate tissues studied using native fluorescence spectroscopy with selective excitation wavelength," J. Biomed. Opt. **15**(4), 047008 (2010).
84. R. R. Alfano, S. J. Wahl, A. Pradhan, and G. C. Tang, "Optical spectroscopic diagnosis of cancer and normal breast tissues," J. Opt. Soc. Am. B **6**(5), 1015 (1989).